CrossMark

Kármán–Howarth solutions of homogeneous isotropic turbulence

L. Djenidi[1],† and R.A. Antonia [1]

[1]Discipline of Mechanical Engineering, School of Engineering, University of Newcastle, Newcastle, 2308 NSW, Australia

The Kármán–Howarth equation (KHEq) is solved using a closure model to obtain solutions of the second-order moment of the velocity increment, S_2, in homogeneous isotropic turbulence (HIT). The results are in good agreement with experimental data for decaying turbulence and are also consistent with calculations based on the three-dimensional energy spectrum for decaying HIT. They differ, however, from those for forced HIT, the difference occurring mainly at large scales. This difference is attributed to the fact that the forcing generates large-scale motions which are not compatible with the KHEq. As the Reynolds number increases, the impact of forcing on the small scales decreases, thus allowing the KHEq and spectrally based solutions to agree well in the range of scales unaffected by forcing. Finally, the results show that the two-thirds law is compatible with the KHEq solutions as the Reynolds number increases to very large, if not infinite, values.

Key words: turbulence theory, isotropic turbulence

1. Introduction

In 1941 Kolmogorov (1941*a*) used dimensional arguments to derive the two-thirds law, $S_2 = \overline{(u(x, t) - u(x + r, t))^2} = C_K(\bar{\epsilon} r)^{2/3}$ (u is the velocity fluctuation, $\bar{\epsilon}$ and r are the mean kinetic energy dissipation rate and spatial increment, respectively, t is time and the overbar represents spatial averaging). In the same year, Kolmogorov (1941*b*) derived the four-fifths law, $S_3 = \overline{(u(x, t) - u(x + r, t))^3} = -(4/5)\bar{\epsilon} r$, from the Kármán–Howarth equation (Von Kármán & Howarth 1938) (hereafter denoted KHEq) expressed in terms of S_2 and S_3 (e.g. Saffman 1968; Danaila *et al.* 1999; Hill 2001):

$$S_3 - 6\nu \frac{\partial S_2}{\partial r} + \frac{3}{r^4} \int_0^r r'^4 \frac{\partial S_2}{\partial t} dr' = -\frac{4}{5} \bar{\epsilon} r, \qquad (1.1)$$

† Email address for correspondence: lyazid.djenidi@newcastle.edu.au

where the second and third terms (the latter hereafter denoted $-Z_r$ for convenience) on the left-hand side account for the effects of the viscosity (mainly dominant in the dissipative range) and the large-scale variations or inhomogeneities, i.e. the integral term. Assuming that both terms are negligibly small in a range of scales excluding both dissipative and large scales when the Reynolds number is infinitely large, Kolmogorov (1941*b*) dropped these terms to obtain the four-fifths law. Further, in 1962 Kolmogorov (1962) attempted to correct his 1941 theory or K41 in order to account for a remark made by Landau (see Landau & Lifshitz 1987) who stated that the slow large-scale variations of the energy dissipation ϵ prevent the universality of small-scale turbulence. Kolmogorov proposed in the 1962 theory, commonly referred to as K62, the following relation for S_2:

$$S_2 = C_2(x, t)(\bar{\epsilon} r)^{2/3} \left(\frac{r}{L}\right)^{\alpha}, \qquad (1.2)$$

where $C_2(x, t)$ is a constant which may depend on the macrostructure of the flow, L is an integral length scale representative of the large-scale structures of the flow and α is a universal positive constant (i.e. independent of Reynolds number and flow). Interestingly, he assumed that the four-fifths law remains valid without any demonstration. Following K62, (1.2) has been generalised as

$$S_n = C_n(x, t)(\bar{\epsilon} r)^{n/3} \left(\frac{r}{L}\right)^{\alpha_n}, \qquad (1.3)$$

which is often written as

$$S_n = A_n(x, t) \left(\frac{r}{L}\right)^{\zeta_n}, \qquad (1.4)$$

where α_n and $\zeta_n = n/3 + \alpha_n$ are positive real numbers; $\alpha_n \neq 0$ and $\zeta_n \neq n/3$, except for $n = 3$ for which $\alpha_3 = 0$ and $\zeta_3 = 1$. There is no doubt that K62 has shaped the current dominant view of the behaviour of small-scale turbulence. This view is strongly supported by direct numerical simulations (DNS) of forced stationary three-dimensional periodic box turbulence. The support, however, is mostly based on the empirical determination of the power-law exponents ζ_n in finite-Reynolds-number turbulent flows where one cannot ignore the large-scale contribution in the KHEq (1.1). In this context, it is pertinent to revisit our view of the small-scale turbulence behaviour, particularly when the Reynolds number is not infinitely large.

In the present work we assess the behaviour of S_2 based on the solutions of the KHEq when the Reynolds number is finite, and in particular the main objective is to ascertain the possible influence of the large-scale motion on S_2. In that respect, the aim is similar to that in a recent paper (Meldi, Djenidi & Antonia 2021) which assessed the effect of forcing on S_2 and S_3 in the spectral domain by solving the Lin equation using an eddy-damped quasi-normal model (EDQNM). It also extends the scope of a previous paper by the present authors (Djenidi & Antonia 2020). To solve the equation, a closure model for S_3 (Djenidi & Antonia 2020, 2021) is used. Results based on the KHEq not only comply with the Navier–Stokes equations, from which the KHEq is derived, but are well suited to assess the impact of the large-scale motion on S_2, thus at the same time addressing Landau's remark; indeed, the large-scale variations imposed by the large-scale motion are explicitly accounted for by the third term on the left-hand side of (1.1). The present paper is organised as follows. In § 2, the KHEq solutions are presented and compared with DNS data of forced homogeneous isotropic turbulence (HIT) in a three-dimensional periodic box. It is shown that this comparison reveals a paradox concerning the behaviour of S_2 even though both the KHEq and DNS use the same external forcing; in § 3, a resolution to that paradox is offered. Finally a concluding discussion is given in § 4.

2. Kármán–Howarth solutions for S_2

To solve (1.1) as in Djenidi & Antonia (2021, 2020), we use a gradient-type closure with an eddy viscosity formulation:

$$S_3 = -\nu_T \frac{\partial S_2}{\partial r} = -C_{S_3} \frac{(S_2)^2}{\bar{\epsilon}} \frac{\partial S_2}{\partial r}, \qquad (2.1)$$

where $C_{S_3} = (6/5C_K^3)$ and C_K is a constant. The use of an eddy viscosity approximation is not new and its suitability in relation to (1.1) has already been tested (e.g. Domaradzki & Mellor 1984; Oberlack & Peters 1993; Baev & Chernykh 2010; Thiesset *et al.* 2013). The expression of the eddy viscosity, ν_T, in (2.1) differs from those reported in the literature. Djenidi & Antonia (2021) showed that the present expression of ν_T, which does not make any assumption regarding the behaviour of S_2, is valid regardless of whether or not the model takes into account the intermittency of ϵ. This is in line with the commonly accepted fact that S_3 should not be affected by the phenomenon of the intermittency of ϵ, often denoted internal intermittency. After dropping the viscous term (second term on the left-hand side of (1.1)), substituting (2.1) in (1.1) and integrating, we obtain

$$S_2 = C_K (\bar{\epsilon} r)^{2/3} (1 - B_r)^{1/3}, \qquad (2.2)$$

with $B_r = -(5/2\bar{\epsilon} r^2) \int^r Z_{r'} \, dr'$. We can rewrite (2.2) as

$$S_2 = C_K(\tilde{\epsilon}_{r,2} r)^{2/3}, \qquad (2.3)$$

where $\tilde{\epsilon}_{r,2} = \bar{\epsilon}(1 - B_r)^{1/2}$. Interestingly, (1.1) can be written as follows when the dissipative range is ignored:

$$S_3 = \tfrac{4}{5}\bar{\epsilon} r (1 - T_r), \qquad (2.4)$$

where $T_r = (5/4\bar{\epsilon} r)Z_r$. Similarly to S_2 we can write (2.4) as

$$S_3 = \tfrac{4}{5}\tilde{\epsilon}_{r,3} r, \qquad (2.5)$$

where $\tilde{\epsilon}_{r,3} = \bar{\epsilon}(1 - T_r)$. It is important to remember that (2.4) is simply equivalent to (1.1) in the range of scales beyond the dissipative range; i.e. no modelling is involved in (2.4), conversely to (2.2) whose derivation involves a closure model for S_3. If there is a range of scales over which $Z_r \to 0$, the two-thirds and four-fifths laws of K41 are restored. Expressions (2.2) and (2.4) describe the behaviour of S_2 and S_3 in the range of scales beyond the dissipative range and show that the energy-containing large-scale structures impact on these quantities. Since the form of Z_r is not universal (the large-scale motion varies from flow to flow), S_2, as remarked by Landau, but also S_3 will not be universal. Expressions (2.2) and (2.4) can be easily tested against DNS data of three-dimensional periodic forced HIT. In this case, we follow Gotoh, Fukayama & Nakano (2002) and replace the integral term of (1.1) by a new term to mimic steady-state forcing which has the following expression (Gotoh *et al.* 2002):

$$Z_r = 12r \int_0^\infty \left(\frac{1}{15} + \frac{\sin kr}{(kr)^3} + 3\frac{\cos kr}{(kr)^4} - 3\frac{\sin kr}{(kr)^5} \right) F(k) \, dk, \qquad (2.6)$$

where $F(k)$ is a constant external force applied in the spectral domain such as $\int_0^\infty F(k) \, dk = \bar{\epsilon}$ and is localised in a narrow range of low wavenumbers, $k_{f,1} \leqslant k \leqslant k_{f,2}$; thus, $F(k) = \bar{\epsilon}/(k_{f,2} - k_{f,1})$. Figure 1 shows distributions of $(4/5 - Z_r)/(\bar{\epsilon} r)$, which is equal to $S_3/(\bar{\epsilon} r)$, for different values of the Taylor microscale Reynolds number, Re_λ,
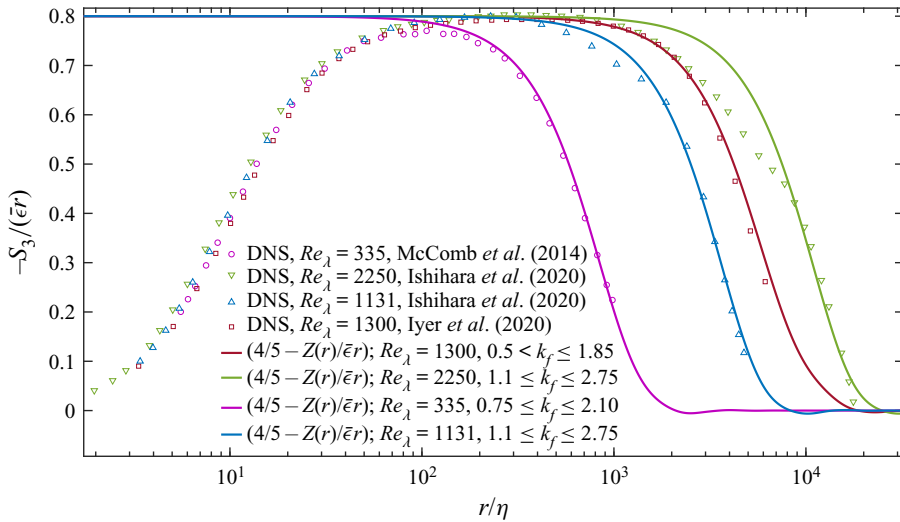
Figure 1. Distributions of $-S_3$ based on (2.4). Symbols: forced HIT DNS data for $-S_3/(\bar{\epsilon}r)$.

ranging from 335 to 2250. To calculate $F(k)$, $\bar{\epsilon}$ is obtained from DNS data (McComb *et al.* 2014; Ishihara *et al.* 2020; Iyer, Sreenivasan & Yeung 2020) whose distributions of S_3 are also shown in the figure. The values of $k_{f,1}$ and $k_{f,2}$ used to calculate Z_r have been selected to match those of the DNS and to align the calculations of Z_r with that from the DNS; the second criterion is based on the fact that when r/η increases, Z_r approaches $(4/5)\bar{\epsilon}r$. Ignoring the dissipative region, which is excluded from (2.4), the present calculated distributions of S_3 agree well with the DNS data. Notice the rather unexpected behaviour of S_3 for the DNS data at $Re_\lambda = 2250$ in the range $1000 \leqslant r/\eta \leqslant 8000$. Indeed, one expects the data to lie above those for $Re_\lambda = 1300$. Overall, the good agreement between the calculations and DNS data gives confidence in the use of (2.6) to calculate S_2 using (2.2). The results are reported in figure 2; we used $C_K = 2.075$, the same value as used by Djenidi & Antonia (2021, 2020), which is close to the generally assumed value of 2. The distribution represented by the cross symbols is the same as that represented by the square symbols, but with $\bar{\epsilon}$ adjusted to bring it into line with the rest of the DNS distributions in the dissipative range; we used the information in table 1 of Yeung, Zhai & Sreenivasan (2015) which provided the data for Iyer *et al.* (2020) whose figure 3, from which we extracted the data, shows $S_2/2u'^2$ as function of r/L. The present calculated distributions follow rather nicely the DNS data for $r/\eta \geqslant 60$. However, for $r/\eta \leqslant 60$ (the dissipative range) the present calculation deviates from the DNS. This is expected since (2.2) ignores the dissipative range. Since it is believed that in the dissipative range $(0 \leqslant r/\eta \leqslant 30)$ S_2 is universal (independent of the Reynolds number), we highlight this region in figure 2 with a solid black line. Note that the exact upper limit of this range is yet to be determined. For this reason we used the fact that the DNS data collapse well for $0 \leqslant r/\eta \leqslant 100$ and drew the black line up to $r/\eta = 100$; for convenience, we denote the range $0 \leqslant r/\eta \leqslant 100$ as the universal dissipative range.

In order to determine whether a better agreement can be obtained between the calculation and DNS, we solved (1.1) using the model (2.1) in the following manner:

$$S_2(r + \Delta r) = S_2(r) + \frac{\left\{ \frac{4}{5}\bar{\epsilon}r - Z_r \right\} \Delta r}{6\nu + C_{S_3}S_2(r)^2/\bar{\epsilon}}, \qquad (2.7)$$
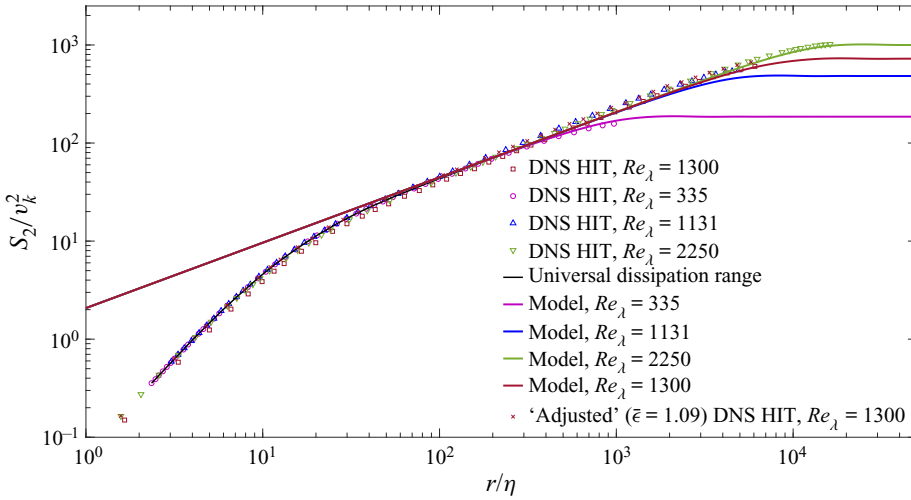
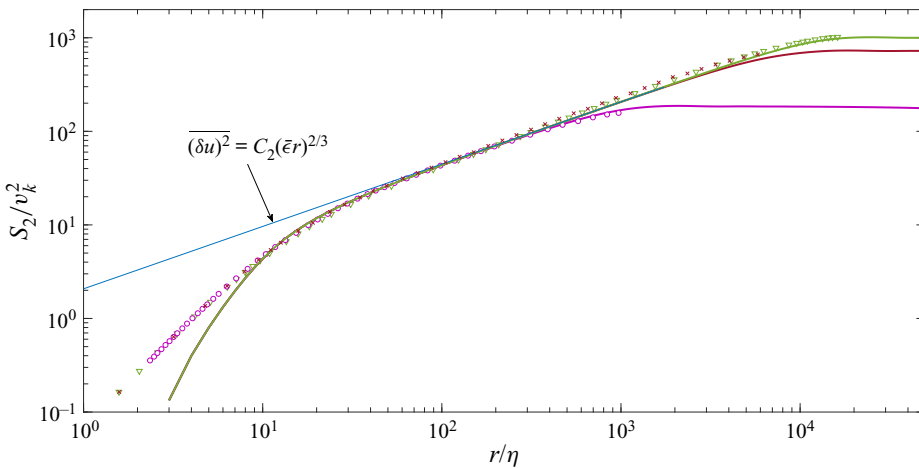Figure 2. Distributions of S_2 based on (2.2). Solid lines and symbols are as in figure 1.

Figure 3. Distributions of S_2 based on the solutions of (1.1). Solid lines and symbols are as in figure 2.

with the boundary condition $S_2 = 0$ at $r = 0$. The results are reported in figure 3 which shows that the agreement between the DNS data and the numerical solution of (1.1) based on (2.7) is extended down to the region $r/\eta \geqslant 10$ as compared to $r/\eta \geqslant 60$ when using (2.2). The good agreement between solutions of (1.1) and DNS is also illustrated in figure 4 which shows distributions of $6\nu(\partial S_2/\partial r)$ (obtained after solving the KHEq using (2.7)) and Z_r from the present calculations and DNS data at $Re_\lambda = 1300$. The Z_r distribution of the DNS data is obtained through a balance of (1.1). There is good agreement between the DNS and the present calculation, although we observe the expected difference in the distributions of $6\nu(\partial S_2/\partial r)$ for $r/\eta \leqslant 10$ since the present solution of S_2 deviates from the DNS in that region. Note that difficulties associated with digitising the DNS data result in a large scatter in Z_r as r/η approaches zero; further, the values of Z_r are sufficiently small in this region so as not to affect the calculations.
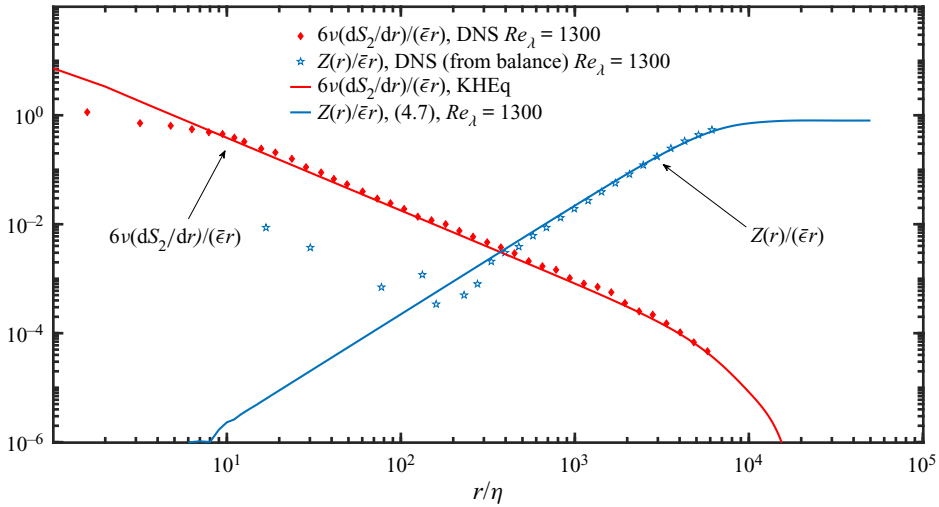
Figure 4. Distributions of Z_r and $6\nu(\partial S_2/\partial r)$ normalised by $\bar{\epsilon}r$.
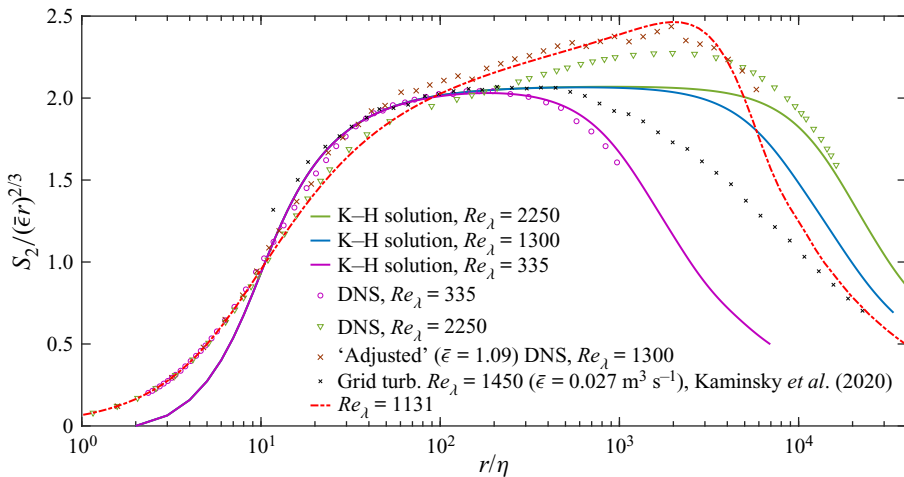

Figure 5. Distributions of $S_2/(\bar{\epsilon}r)^{2/3}$. Solid lines and symbols are as in figure 2. Black crosses: grid turbulence data at $Re_\lambda = 1450$ (Kaminsky *et al.* 2020). Red dash-dotted line: EDQNM, $Re_\lambda = 1131$.

While the comparison between the present calculation and DNS data suggests good agreement, one can nevertheless notice that the DNS data for $Re_\lambda = 1100$, 1300 and 2250 lie slightly above the calculations for $r/\eta \geqslant 200$ before S_2 reaches its constant value at large r/η where it must be $2u'^2$. This difference is more emphatically illustrated in figure 5 which shows the distributions of S_2 of figure 3 normalised by $(\bar{\epsilon}r)^{2/3}$. The decaying grid turbulence data of Kaminsky *et al.* (2020) at $Re_\lambda = 1450$ are added. The value of $\bar{\epsilon}$ reported by Kaminsky *et al.* (2020) has been adjusted so that S_2 (before normalising by $(\bar{\epsilon}r)^{2/3}$) aligns with the other DNS data in the region $10 \leqslant r/\eta \leqslant 100$. The deviation of the present calculated distributions from the DNS data in the region $r/\eta \leqslant 10$ is expected, as explained earlier. The calculations show that, as r/η increases, $S_2/(\bar{\epsilon}r)^{2/3}$ approaches a region over which it varies very slowly before decreasing again. The extent of this region increases with the Reynolds number. While the DNS data at $Re_\lambda = 335$ and the

grid turbulence data behave similarly, the DNS data at $Re_\lambda = 1300$ and 2250 exhibit an 'overshoot' when compared to the calculated distributions. A similar behaviour is seen for the data of Ishihara *et al.* (2020) even when Re_λ is as small as 675. Interestingly, the numerical simulations of HIT up to $Re_\lambda = 10^6$ based on an EDQNM (Meldi *et al.* 2021) show the existence of a similar overshoot when HIT is forced (an example is shown in the figure); the overshoot is not observed for decaying HIT.

The above comparison between the present calculations and the DNS data raises a paradox which, for convenience, is hereafter referred to as the S_2 paradox. Indeed, even though the calculations and the DNS (and EDQNM) use the same forcing, there is no overshoot in the former. This is disconcerting since both the calculations and DNS have similar S_3 and Z_r distributions in the region beyond the dissipative range, as seen in figures 1 and 4. This paradox and its resolution are considered in the next section.

3. The S_2 paradox

In the present calculations, the closed form of the KHEq is solved to obtain S_2. However, S_2 can also be calculated, as done in EDQNM and DNS, from the three-dimensional energy spectrum, $E(k)$, as follows:

$$S_2 = 4 \int_0^\infty E(k) \left(\frac{1}{3} - \frac{\sin kr - kr \cos kr}{(kr)^3} \right) \mathrm{d}k, \tag{3.1}$$

where k is the wavenumber. For the purpose of the analysis, a theoretical spectrum with and without forcing is considered. The unforced spectrum is that of Pope (2000):

$$E(k) = C\bar{\epsilon}^{2/3} k^{-5/3} f_L(kL) f_\eta(k\eta), \tag{3.2}$$

where $C = 1.5$,

$$f_L(kL) = \left(\frac{kL}{[(kL)^{1.5} + c_L]^{1/1.5}} \right)^{2/3} k^{5/3+p} \tag{3.3}$$

and

$$f_\eta(k\eta) = \exp(-\beta([(k\eta)^4 + c_\eta^4]^{1/4} - c_\eta)), \tag{3.4}$$

with $p = 2$, $c_L = 6.78$, $\beta = 5.3$ and $c_\eta = 0.4$. To emulate a forced spectrum we simply use

$$E_f(k) = \left(1 + \frac{\gamma}{k} \right) E(k), \tag{3.5}$$

where γ can take any positive value to change the forcing intensity. This is simple but, as will be seen, sufficient to illustrate the effect of a low-wavenumber forcing on the calculation of S_2 via (3.1). Figure 6 shows the unforced and forced spectra for two largely different kinematic viscosity values that lead to a significant Reynolds number difference. The figure (inset) also reports the DNS data for forced HIT of Ishihara *et al.* (2016). We have used their data of $\bar{\epsilon}$ and L; for $Re_\lambda = 2297$ we used their value of $\nu = 4.1 \times 10^{-6}$; for $Re_\lambda = 7.264 \times 10^4$ we simply reduced the viscosity to $\nu = 4.1 \times 10^{-9}$, while $\bar{\epsilon}$ and L are unchanged. When forcing is applied, the forced spectra differ from the unforced spectra in the low-wavenumber region. This indicates that (3.5) emulates relatively well a spectrum of forced HIT (seen in the inset), and can represent the spectra obtained in the DNS and EDQNM simulations of forced HIT. Thus, both forced and unforced spectra can now be used to compute S_2 using (3.1) and the results are reported in figure 7 showing the distributions $S_2/(\bar{\epsilon}r)^{2/3}$ for different values of γ. We also show the EDQNM data for
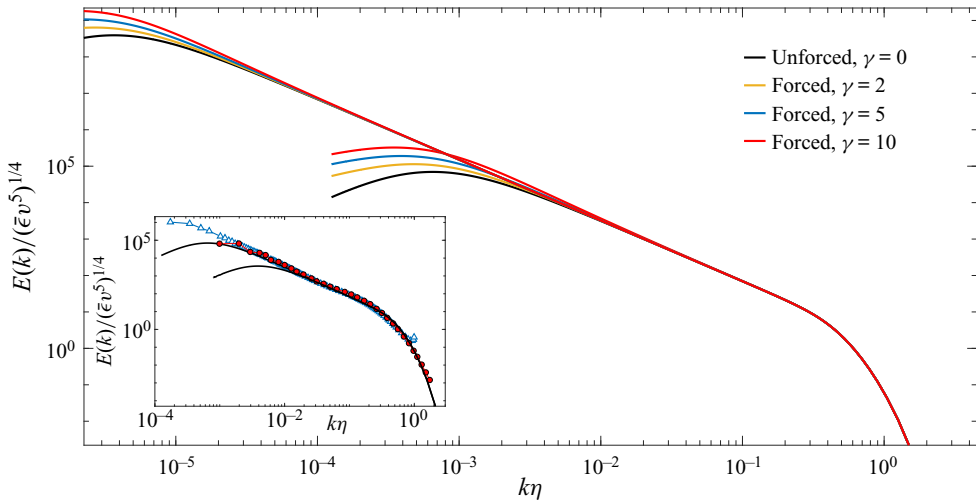
Figure 6. Unforced ($\gamma = 0$) and forced ($\gamma = 2$, 5 and 10) three-dimensional energy spectra for $Re_\lambda = 2297$ (thick lines) and 7.264×10^4 (thin lines). Inset: DNS data of Ishihara *et al.* (2016). Red circles, $Re_\lambda = 675$; blue triangles, $Re_\lambda = 2297$; black lines, unforced spectra for $Re_\lambda = 675$ and 2297.

$Re_\lambda = 10^4$ of Meldi *et al.* (2021). In (3.2), C is supposed to be equal to the Kolmogorov constant C_K. However, the value of 1.5 used in (3.2) is lower than the assumed value of $C_K \simeq 2$. Here, we also use $C = 1.5$ since, in combination with the other (fitting) constants p, c_L, β and c_η, it yields good agreement with DNS spectra as shown in figure 6. The actual value of C is not important as it does not alter the shapes of the S_2 curves calculated with (3.1), which are the focus here, and as illustrated in figures 7(*a*) and 7(*b*) where we used $C = 1.5$ and 1.63, respectively. The results of figure 7 illustrate the impact of forcing on S_2. Forcing increases the magnitude of $S_2/(\bar{\epsilon}r)^{2/3}$ when compared to the unforced spectra and can lead to a significant overshoot. Note though that the impact of forcing is practically negligible in the region $r/\eta \leqslant 10$. The effect of forcing becomes important for $r \geqslant 10\eta$ and $r \geqslant 1000\eta$ at lower and larger Reynolds numbers, respectively. The plots of figure 7 indicate that the larger the forcing intensity the deeper into the small scales its effect will be felt. It also indicates that the larger the Reynolds number the weaker this effect is on the small scales. Taking these considerations into account, one can argue that the DNS data shown in figure 5 present a trend towards $S_2/(\bar{\epsilon}r)^{2/3}$ and that higher-Reynolds-number DNS may confirm this trend.

The message of figure 7 is clear: the external spectral forcing applied at lower wavenumbers can lead to an overshoot in the $S_2/(\bar{\epsilon}r)^{2/3}$ distributions when compared to the no forcing case. This nevertheless does not yet explain the S_2 paradox. But it should be recalled that the KHEq has been developed in the context of a decaying turbulence which is isotropic at all scales of motion. In this context, not only should the large-scale motion be isotropic, but its energy should decay in time. Thus, its contribution, i.e. the third term on the left-hand side of (1.1), also decays in time. Replacing this term by another one to emulate a steady-state isotropic turbulence thus changes the nature of the equation. For example, the integral term, which is a cumulative term, depends on S_2, while the replacing term (2.6) is neither cumulative nor S_2-dependent. This reminds us that the extra term commonly added to the Navier–Stokes equations (from which, we should recall, (1.1) is derived) to emulate external forcing at large scales is unnatural (Lamorgese, Caughey & Pope 2005). It is worth remembering that its use is justified on the basis that it has little
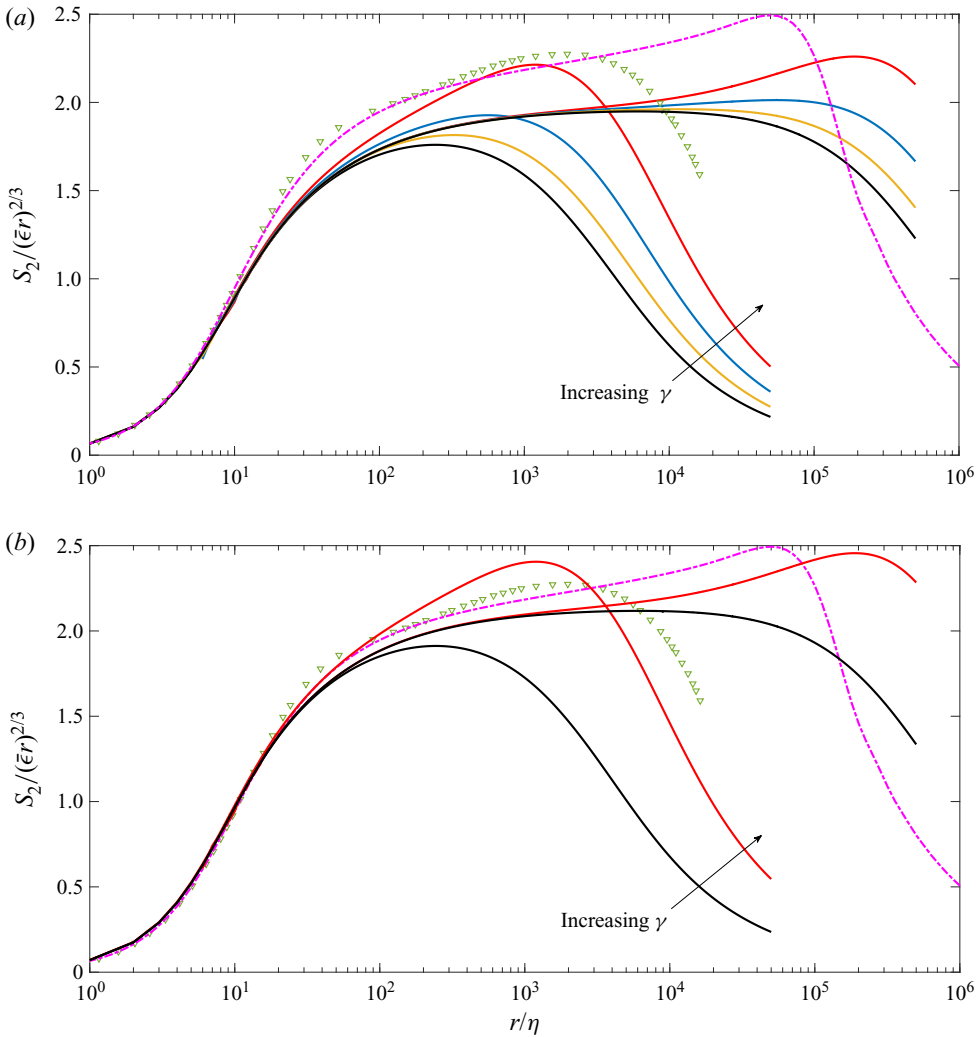
Figure 7. Distributions of $S_2/(\bar{\epsilon}r)^{2/3}$ computed with unforced and forced spectra. Lines are the same as in figure 6. Triangles, DNS data of Ishihara *et al.* (2020), $Re_\lambda = 2297$; pink dash-dotted line, EDQNM data of Meldi *et al.* (2021), $Re_\lambda = 10^4$. The arrow indicates the direction of increasing γ. (*a*) Parameter C in (3.2) is equal to 1.5; (*b*) $C = 1.63$ and only the cases for $\gamma = 0$ and 10 are shown with the DNS and EDQNM data.

effect on the small-scale statistics. Clearly, the results of figure 7 contradict this view, particularly when the Reynolds number is not large enough. The change in the nature of the KHEq when the forcing term is added can be illustrated by considering the following equation in the region beyond the dissipative range, where the viscous term in (1.1) can be dropped:

$$S_3 - Z_r = -\tfrac{4}{5}\bar{\epsilon}r. \tag{3.6}$$

For decaying isotropic turbulence, Z_r is given by the integral term in (1.1) and (3.6) is the transport equation of S_2 with S_3 unknown. On the other hand, if Z_r is given by (2.6), then (3.6) is not a transport equation for S_2 since S_2 does not appear in the equation. In fact, (3.6) can be used to obtain S_3, as done in § 2, irrespective of S_2 which, as far as this equation is concerned, is undetermined and thus can have any value. This remark concerning the
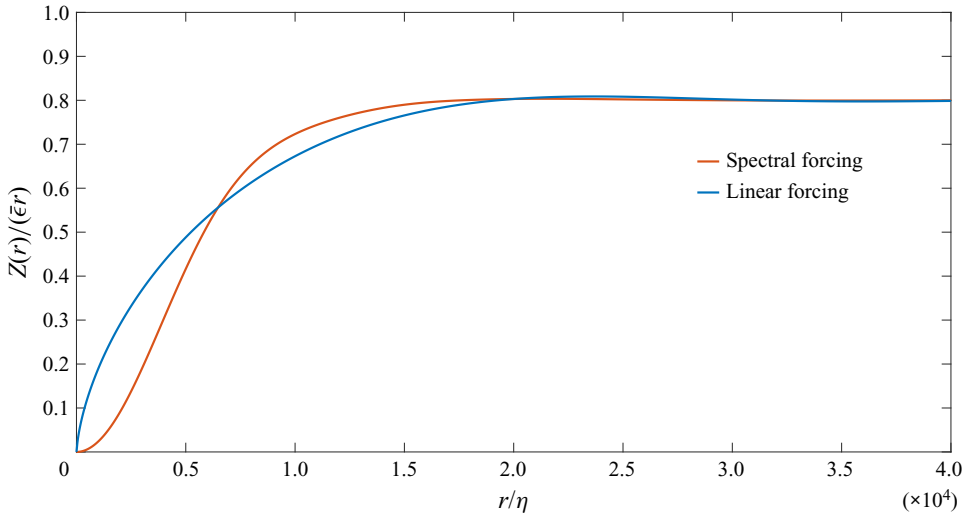
Figure 8. Distributions of $Z_r/(\bar{\epsilon}r)$ computed via (3.7) (linear forcing, blue line) and (2.6) (spectral forcing, red line).

change in the nature of the KHEq echoes Pope's (2000) reminder that the large-scale energy-containing motions generated in the spectral domain by low-wavenumber forcing are unnatural and not governed by the Navier–Stokes equations. In that context, it is not surprising that the KHEq solutions do not agree with numerical simulations where a turbulence field is generated by an external forcing such as in DNS and EDQNM calculations. Only if the Reynolds number is large enough can the KHEq, DNS and EDQNM solutions be in agreement in the dissipative and scaling ranges, as indeed figures 5 and 7 would suggest.

We complete this section by solving the KHEq where Z_r is given by the linear isotropic forcing used by Lundgren (2003):

$$Z_r = \frac{2\bar{\epsilon}}{u'^2} \frac{1}{r^4} \int_0^r s^4 S_2 \, \mathrm{d}s. \tag{3.7}$$

Lundgren suggests that this forcing is equivalent to a uniform spectral forcing at all wavenumbers and can allow comparison with decaying HIT. Notice the cumulative aspect of this expression, mimicking the integral term in (1.1). Figure 8 shows Z_r for both linear and spectral forcing. Both types of forcing lead to the correct limit, $Z_r = (4/5)(\bar{\epsilon}r)$, as they should, at large r/η but they result in significantly different behaviours as r/η decreases. They decrease at different rates with decreasing r/η. For example, as r/η decreases, Z_r remains larger for the spectral than for the linear forcing until $r/\eta \simeq 0.6 \times 10^4$. Below this value, Z_r is smaller with the linear forcing. One can expect that this behaviour should be reflected in the distributions of S_2. This is indeed observed in figure 9 which shows distributions of S_2 normalised by v_K. As the large scales are approached, the calculations based on the spectral forcing yield systematically higher values of S_2 than when the linear forcing is used. This was also observed by Lundgren (2003), although the observation was made with regard to the approach to the four-fifths law. Notice that in an attempt to improve the calculation in the dissipative range, we used the boundary condition $S_2 = (1/15\nu)\bar{\epsilon}r^2$ at $r = \eta$, which is the correct solution of the KHEq in the dissipative range where the first and third terms on the left-hand side of (1.1) are negligibly small. A comparison with figure 3 indicates that this simple change of boundary condition improves the calculation in
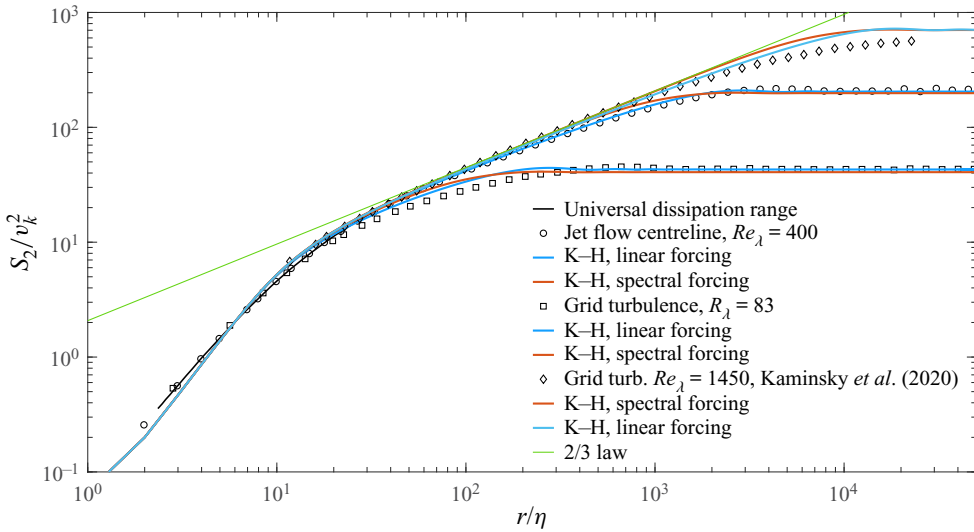
Figure 9. Distributions of S_2 computed via (1.1) with spectral forcing (red lines) and linear forcing (blue lines). Symbols are experimental data of grid turbulence and round jet.

the dissipative range. Also reported in figure 9 are the experimental data of grid turbulence (Djenidi, Kamruzzaman & Antonia 2015; Kaminsky *et al.* 2020) and round jet centreline (Djenidi *et al.* 2016). Adding a forcing term to the Navier–Stokes equations is equivalent to introducing energy. This energy is then distributed among all scales of motion. But, as illustrated by Z_r, this distribution is not uniform among the scales of motion; the larger the scales the more energy they receive. This is well reflected in the distributions of S_2/v_K^2. The calculated (forced) distributions exhibit higher values of S_2/v_K^2 than the measured (decaying) distributions in the range of scales delimited by the dissipative range and the very large scales where S_2 becomes constant. Interestingly, the agreement between calculation and measurement is better for the jet flow than grid turbulence, suggesting that the large-scale contribution is stronger in the former flow.

4. Concluding discussion

A closed form of the KHEq is solved to investigate the behaviour of the second-order velocity structure function, S_2, in HIT at finite Reynolds numbers. The closure model is based on a gradient type with an eddy viscosity formulation proposed by Djenidi & Antonia (2021). The results are in good agreement with experimental data (figure 9). Further, they indicate that when the Reynolds number is large, S_2 behaves like $(\bar{\epsilon}r)^{2/3}$ in a range of scales beyond the dissipative range and well before the scale range where S_2 becomes constant, thus supporting the existence of a two-thirds law when the Reynolds number is very, if not infinitely, large. However, comparison with the DNS data for forced HIT reveals a paradox: while both the KHEq and DNS use the same isotropic spectral forcing, the DNS data exhibit larger values of S_2 than the KHEq solutions in the region where $S_3/(\bar{\epsilon}r)$ starts to decrease with increasing r (figure 1), which is illustrated by an overshoot in $S_2/(\bar{\epsilon}r)^{2/3}$ (figure 5). Calculations of S_2 via the energy spectrum (3.1) reveal similar overshoots in $S_2/(\bar{\epsilon}r)^{2/3}$ when forced spectra are used (figure 7); also, the stronger the forcing intensity the larger the magnitude of the overshoot. These results strongly suggest that the overshoot exhibited by the DNS data is associated with the forced energy

spectrum. As the Reynolds number increases, and for a given spectral forcing applied at the same low wavenumbers, the overshoot shifts to larger values of r/η allowing S_2 to approach its infinite-Reynolds-number behaviour, i.e. $(\bar{\epsilon}r)^{2/3}$, in the scaling range. This discussion about the overshoot in the distributions of $S_2/(\bar{\epsilon}r)^{2/3}$ raises a pertinent question: why do the DNS data for $S_3/(\bar{\epsilon}r)$ not show an overshoot when forcing is applied? Moment S_3 is associated with the transfer of energy, not with the energy itself, so that the actual mechanism of energy transfer among scales is the same regardless of whether the energy spectrum is forced or not; there is simply more energy to transfer when forcing is used.

An interesting point that stems from the present study concerns the two-thirds law. The KHEq solutions clearly show that as long as turbulence is isotropic at all scales of motion, this law can be well approximated at large Reynolds numbers; it is better approximated in forced than in decaying turbulence, as seen in figure 9. Also, the presence of the large-scale anisotropy disrupts this. Indeed, the effect of this anisotropy can penetrate deep into the small scales, particularly if the Reynolds number is not large. This unfortunately complicates the interpretation of comparisons between the (isotropic) Kármán–Howarth predictions and the actual results in anisotropic flows.

Finally, the present results, and in particular the calculations of S_2 based on the forced three-dimensional energy spectrum, suggest that the current DNS data are not inconsistent with a trend towards the two-thirds law. It is possible that the current DNS Reynolds numbers are not large enough to avoid the effect of forcing on the small scales beyond the dissipative range and thus disrupting the behaviour of S_2 in the so-called scaling range; this effect increases as the size of the scale increases. DNS data at much larger Reynolds numbers than the current ones will certainly help clarify the issue of how forcing affects the scaling range.

Declaration of interests. The authors report no conflict of interest.

Author ORCIDs.
L. Djenidi https://orcid.org/0000-0001-8614-3595.

REFERENCES

BAEV, M.K. & CHERNYKH, G.G. 2010 On Corrsin equation closure. *J. Engng Thermophys.* **19** (3), 154–169.
DANAILA, L., ANSELMET, F., ZHOU, T. & ANTONIA, R.A. 1999 A generalization of Yaglom's equation which accounts for the large-scale forcing in heated decaying turbulence. *J. Fluid Mech.* **391**, 359–372.
DJENIDI, L & ANTONIA, R.A. 2020 Assessment of large-scale forcing in isotropic turbulence using a closed Kármán–Howarth equation. *Phys. Fluids* **32** (5), 055104.
DJENIDI, L. & ANTONIA, R.A. 2021 Modelling the third-order velocity structure function in the scaling range at finite Reynolds numbers. *J. Math. Phys.* **62** (8), 083102.
DJENIDI, L., ANTONIA, R.A., LEFEUVRE, N. & LEMAY, J. 2016 Complete self-preservation on the axis of a turbulent round jet. *J Fluid Mech.* **790**, 57–70.
DJENIDI, L., KAMRUZZAMAN, M.. & ANTONIA, R.A. 2015 Power-law exponent in the transition period of decay in grid turbulence. *J. Fluid Mech.* **779**, 544–555.
DOMARADZKI, J.A. & MELLOR, G.L. 1984 A simple turbulence closure hypothesis for the triple-velocity correlation functions in homogeneous isotropic turbulence. *J. Fluid Mech.* **140**, 45–61.
GOTOH, T., FUKAYAMA, D. & NAKANO, T. 2002 Velocity field statistics in homogeneous steady turbulence obtained using a high-resolution direct numerical simulation. *Phys. Fluids* **14** (3), 1065–1081.
HILL, R.J. 2001 Equations relating structure functions of all orders. *J. Fluid Mech.* **434**, 379–388.
ISHIHARA, T., KANEDA, Y., MORISHITA, K., YOKOKAWA, M. & UNO, A. 2020 Second-order velocity structure functions in direct numerical simulations of turbulence with R_λ up to 2250. *Phys. Rev. Fluids* **5** (10), 104608.
ISHIHARA, T., MORISHITA, K., YOKOKAWA, M., UNO, A. & KANEDA, Y. 2016 Energy spectrum in high-resolution direct numerical simulations of turbulence. *Phys. Rev. Fluids* **1** (8), 082403.

Iyer, K.P., Sreenivasan, K.R. & Yeung, P.K. 2020 Scaling exponents saturate in three-dimensional isotropic turbulence. *Phys. Rev. Fluids* **5** (5), 054605.

Kaminsky, J., Birnir, B., Bewley, G.P. & Sinhuber, M. 2020 Reynolds number dependence of the structure functions in homogeneous turbulence. *J. Nonlinear Sci.* **30** (3), 1081–1114.

Kolmogorov, A.N. 1941*a* The local structure of turbulence in incompressible viscous fluid for very large Reynolds number. *Dokl. Akad. Nauk SSSR* **30**, 299–303. (see also *Proc. R. Soc. Lond.* A (1991) **434**, 9–13).

Kolmogorov, A.N. 1941*b* Dissipation of energy in the locally isotropic turbulence. *Dokl. Akad. Nauk SSSR* **32**, 16–18. (see also *Proc. R. Soc. Lond.* A (1991), **434**, 15–17).

Kolmogorov, A.N. 1962 A refinement of previous hypotheses concerning the local structure of turbulence in a viscous incompressible fluid at high Reynolds number. *J. Fluid Mech.* **13**, 82–85.

Lamorgese, A.G., Caughey, D.A. & Pope, S.B. 2005 Direct numerical simulation of homogeneous turbulence with hyperviscosity. *Phys. Fluids* **17** (1), 015106.

Landau, L.D. & Lifshitz, E.M. 1987 *Fluid Mechanics: Vol 6 of Course of Theoretical Physics*, 2nd English edn revised. Pergamon.

Lundgren, T.S. 2003 Linearly forced isotropic turbulence. In *Annual Review Briefs, Center for Turbulence Research* ADP014826, University of Minnesota.

McComb, W.D., Yoffe, S.R., Linkmann, M.F. & Berera, A. 2014 Spectral analysis of structure functions and their scaling exponents in forced isotropic turbulence. *Phys. Rev.* E **90** (5), 053010.

Meldi, M., Djenidi, L. & Antonia, R.A. 2021 Sensitivity analysis of the second and third-order velocity structure functions to the Reynolds number in decaying and forced isotropic turbulence using the EDQNM model. *Eur. J. Mech. (B/Fluids)* **88**, 229–242.

Oberlack, M. & Peters, N. 1993 Closure of the two-point correlation equation as a basis for Reynolds stress models. *Appl. Sci. Res.* **51** (1–2), 533–538.

Pope, S.B. 2000 *Turbulent Flows*. Cambridge University Press.

Saffman, P.G. 1968 Lectures on homogeneous turbulence. *Top. Nonlinear Phys.* 485–614.

Thiesset, F., Antonia, R.A., Danaila, L. & Djenidi, L. 2013 Kármán–Howarth closure equation on the basis of a universal eddy viscosity. *Phys. Rev.* E **88** (1), 011003.

Von Kármán, T. & Howarth, L. 1938 On the statistical theory of isotropic turbulence. *Proc. R. Soc. Lond.* A **164**, 192–215.

Yeung, P.K., Zhai, X.M. & Sreenivasan, K.R. 2015 Extreme events in computational turbulence. *Proc. Natl Acad. Sci. USA* **112** (41), 12633–12638.